JGR Space Physics

RESEARCH ARTICLE
10.1029/2019JA026768

Relationship Between Global Plasmapause Characteristics and Plasmapause Structures in the Frame of Interchange Instability Mechanism

Mario Bandić[1], Giuliana Verbanac[2], and Viviane Pierrard[3,4]

[1]Astronomical Observatory Zagreb, Zagreb, Croatia, [2]Faculty of science, University of Zagreb, Zagreb, Croatia, [3]Royal Belgian Institute for Space Aeronomy (Space Physics and STCE), Brussels, Belgium, [4]Earth and Life Institute, TECLIM, Université Catholique de Louvain, Louvain-La-Neuve, Belgium

Key Points:
- Interchange instability simulations that employ real *Kp* values and a few types of *Kp* jumps as input provide same plasmapause characteristics
- Statistical plasmapause behavior is successfully explained by considering only three plasmapause structures: plumes, shoulders, and notches
- Global plasmapause evolution in time (azimuthal propagation and MLT sectors of radial deformation) is simplified and systematized

Supporting Information:
- Supporting Information S1
- Figure S1
- Figure S2

Correspondence to:
G. Verbanac,
giuli1.verbanac@gmail.com

Citation:
Bandić, M., Verbanac, G., & Pierrard, V. (2020). Relationship between global plasmapause characteristics and plasmapause structures in the frame of interchange instability mechanism. *Journal of Geophysical Research: Space Physics*, *125*, e2019JA026768. https://doi.org/10.1029/2019JA026768

Received 30 MAR 2019
Accepted 14 SEP 2019
Accepted article online 15 OCT 2019

Abstract Recent studies based on CLUSTER, CRRES, and especially on THEMIS satellite data have revealed the statistical behavior of the global plasmapause such as eastward azimuthal plasmapause propagation and radial plasmapause motion between 21 and 07 magnetic local times (MLTs) most likely at postmidnight. The results are shown to be in a good agreement with characteristics of the plasmapause modeled using interchange instability mechanism. The present study is based on the plasmapause modeled with the mentioned physical mechanism, and it aims to link the observed global plasmapause dynamic with formation and evolution of plasmapause structures. We investigated two plasmapause datasets obtained using real Kp values and certain type of time-dependent changes in the Kp (thereafter Kp jumps) as input in the simulations. The Kp jumps include sharp Kp increase, sharp Kp decrease, short-time burst enhancement (increase-decrease within 3 hr) in Kp, and their combinations in order to obtain plumes, shoulders, and notches, the structures most often observed in the nature. The cross-correlation analyses is applied to the modeled plasmapause and to the geomagnetic Kp index at different 1-hr MLT bins. We have shown that the cross-correlation curves provide deeper insight in the physical processes related to the plasmapause dynamic and evolution. Their behavior is interpreted as the imprint of the plasmapause structure passages through specific MLT sector. Taking into account that the plasmapause in the single events shows very complex and different behaviors, the most important finding of the present study is the simple explanation of what causes global plasmapause motions and deformation in time.

1. Introduction

Plasmapause characteristics including its formation, dynamic, development, and evolution of different structures have been studied by many authors. Most of such studies are based on the individual cases (Gallagher et al., 2005; Goldstein, Burch et al., 2005; Goldstein, Sandel et al., 2005; Horwitz et al., 1990; Pierrard & Stegen, 2008; Pierrard et al., 2008; Sandel et al., 2003; Sheeley et al., 2001; Spasojević et al., 2003). Although the inferred plasmapause characteristics are representative only for a particular single event, these works are important since they have revealed different plasmapause shapes characterized by different structures such as plumes, notches, shoulders, crenulations, channels, and fingers (Darrouzet, Gallagher, et al., 2009).

Recently, statistical behavior of the global plasmapause has been deduced using experimental satellite data (Bandić et al., 2016, 2017; Verbanac et al., 2015, 2018). These works did not follow the formation and time evolution of any plasmapause structures, and the obtained results represent the most probable global plasmapause characteristics. The study by Verbanac et al. (2018) has also performed a statistical comparison of the global behavior of the large statistical plasmapause sample derived from THEMIS satellite observations in the period 2008–2012 and plasmapause that was modeled using the simulation based on interchange instability mechanism (Lemaire & Gringauz, 1998; Pierrard & Stegen, 2008). The response of both the experimental and simulated plasmapause to various solar wind/geomagnetic activity indices (thereafter PP indicators) at different magnetic local times (thereafter MLTs) was investigated by applying the cross-correlation analysis that is shown to be a powerful tool to derive global plasmapause characteristics statistically (Bandić et al., 2017; Verbanac et al., 2015, 2018). In summary, these works analyzed the cross-correlation curves (thereafter CC curves) and suggested a global eastward azimuthal plasmapause

propagation and a radial plasmapause motion (representing plasmapause erosion and expansion) between 21 MLT and 07 MLT, most likely at postmidnight. In the dayside, they found the entirely azimuthal plasmapause propagation. The mean angular velocity of propagation is estimated to be close to the corotation speed at all MLTs for the studied time span. The experimental and modeled plasmapause characteristics are found to be in agreement. Important to note is that plasmapause characteristics obtained using different PP indicators are similar. This further assures the reliability of their findings.

The aim of the present study is to

1. analyze in detail the plasmapause characteristics as obtained in Verbanac et al. (2018). Since the plasmapause dynamics derived from experimental and modeled plasmapause are in accordance, we focus here on the modeled plasmapause.
2. link the global plasmapause dynamic observed in Verbanac et al. (2018) with formation and evolution of plasmapause structures (as observed in individual cases). In this way, for the first time, the development of different structures are statistically included in the process of the plasmapause formation and evolution.

The motivation to bring different structures observed in the nature, such plumes, shoulders, and notches in relationship with plasmapause formation and propagation comes from the facts that (a) these structures can be well reproduced with physical mechanism of interchange instability (Pierrard & Lemaire, 2004) and (b) the structures obtained with interchange instability simulations are quite well in agreement with the plasmapause structures observed by the IMAGE satellite (Pierrard & Cabrera, 2005, 2006; Pierrard et al., 2008).

To achieve the posted aims, we investigated the following plasmapause datasets. The first used dataset is the one obtained by Verbanac et al. (2018) which consists of 41,113 plasmapauses obtained using real Kp values as input in the simulations. The second database contains 26,454 plasmapauses and is developed in the present study. We run the simulations giving as the input the certain type of time-dependent changes in the Kp. These changes in Kp (thereafter Kp jumps) include: sharp Kp increase, sharp Kp decrease, short time burst enhancement (increase-decrease within 3 hr) in Kp, increase-decrease in Kp that occurs within 6 hr, increase-decrease in Kp that occurs within 12 hr. The first three types of Kp jumps are chosen in order to obtain plumes, shoulders and notches, the structures most often observed in the nature, e.g. by Extreme UltraViolet instrument on board the IMAGE spacecraft (Darrouzet, DeKeyser, et al., 2009). The last two types of Kp jumps are included to improve the statistics. Note that in this paper, the notch is referred to the structure obtained when Kp increases and after 3 hr decreases to certain values, the same as defined in Pierrard and Lemaire (2004).

We focus on the explanation of the CC curves obtained when the plasmapause from both plasmapause data sets are cross-correlated with geomagnetic Kp index at different 1-hr MLT bins. More details on used data sets and the CC curves are given in the following sections.

The present study provides deeper insight in the physical meaning of the specific shapes observed in the CC curves. We show that statistically the global processes of the plasmapause dynamics (formation and propagation) can simply be explained by considering a few types of plasmapause structures. In this way, our work pays a way to different investigation approaches, views, and better understanding of the plasmapause dynamics derived from large plasmapause data sets. The great contribution of the obtained results is that the observed structures seen in the nature are successfully taken into account when deducing the global plasmapause characteristics from experimental data set that cover large time span, since the availability of plasmapause snapshots (sequences of plasmapause images) is limited. Moreover snapshots often do not provide the plasmapause at all MLTs.

The paper is organized as follows. In the next section, we explain the data set. Characteristics of the plasmapause modeled by employing Kp jumps are given in section 3. Section 4 provides the analyses of the CC curves. Discussion and conclusion are given in the last section.

2. Data Sets

The following data sets are used in this study: (1) plasmapause obtained from numerical simulations using real Kp values for the period 2008–2012 (thereafter sL_{PP} values); (2) plasmapause obtained from numerical simulations for the specific Kp jumps (thereafter jL_{PP} values); (3) 3-hourly-values of geomagnetic activity index Kp.

The simulations used to create both data sets, (1) and (2), are based on the kinetic description of the interchange motion and instability. The detailed description of this kinetic approach, with direct application to the Earth's plasmasphere is given in Lemaire and Gringauz (1998). Note that here, the plasmasphere is considered as a separate plasma system (independent of other plasma systems in the inner part of the magnetosphere such as ring current and radiation belts). For more theoretical details related to the contribution of different terms (as centrifugal force, gravity, pressure gradients, polarization electric field) in the equations readers are referred to Chapter 5 of that book. The equations for kinetic instabilities are also well explained in André and Lemaire (2006). Different description of the interchange motion and instability relies on the ideal MHD formalism, firstly introduced by Gold (1959). The definitions and differences between these two descriptions are given in Ferriere (2001).

In the theory based on kinetic description of the interchange motion, the plasmapause coincides with a streamline tangent to the Zero Parallel Force surface where the field aligned component of the centrifugal and gravitational accelerations are in balance. Above this surface, the plasma becomes unstable at postmidnight since the convection electric field has the largest value allowing the onset of the plasmapause erosion. The erosion in these MLT sectors is also favored by the maximal interchange velocity (based on kinetic approach of interchange instability) there. This is why the simulations start at 02 MLT. Duration of the simulation is longer than one full cycle, meaning that it runs further than 02 MLT. It continues up to 05 MLT. The branch from 02 MLT to 02 MLT is referred to the first simulation cycle. The extended branch from 02 MLT to 05 MLT belongs to the second simulation cycle. Depending on the geomagnetic activity (if Kp increases or decreases), the second simulation branch is closer or farther from the Earth. The simulations provide the L_{PP} values by considering the magnetospheric convection electric field model E5D (McIlwain, 1986), the associated magnetic field model, and corotation. The input for the simulations is also the geomagnetic index Kp at any chosen date starting at time T_0 (denoted as "DAY 2") and the Kp of the previous day, since Kp is the parameter controlling the E5D electric field. The plasmapause at a specific time is determined by the interchange mechanism and by the history of geomagnetic activity (Kp) during the previous 24 hr.

The E5D electric field does not take into account undershielding, overshielding, and SubAuroral Polarization Streams, but the benefit is that it was deduced from ATS-5 and ATS-6 particle flux measurements at geosynchronous altitude, precisely in the region where the plasmapause is formed. There are other electric field models based on individual events derived by adjusting their parameters to fit the specific observed plasmapause positions (Goldstein et al., 2005; Huba & Sazykin, 2017; Lambour et al., 1997, e.g.). For all individual plasmapause crossings, there is little guarantee that the magnetospheric convection electric field distributions are identical or nearly similar to each other. Thus, the E5D model used as the input electric field for the simulations is not expected to fit all situations at any time. This model is unlikely to be representative for all plasmapause erosion/refiling events, not more than any other empirical models. Nevertheless, this study and our previous studies (Bandić et al., 2016, 2017; Verbanac et al., 2015, 2018) have all shown that the E5D model is reliable, at least in the statistical sense, since with this electric field and kinetic approach of interchange instability, we obtained the global plasmapause characteristics that are in agreement with experimental data. Moreover, the agreement has been achieved using different satellite data (CLUSTER, CRRES, and THEMIS).

The first data set is derived by Verbanac et al. (2018), and it consists of 41,113 sL_{PP} values embracing time span 2008–2012. For details, the readers are referred to their paper.

The second data set, jL_{PP} values, is developed in the present study. To obtain the jL_{PP} values, five types of time-dependent changes in the Kp are given as the input in the simulations. Within each of these five types, we investigated 8 different Kp jumps as follows:

1. Sharp Kp increase. Kp increases from the certain value at T_0 to higher certain value that afterwards remains constant. We analyzed jL_{PP} values obtained for the following Kp jumps: 0.3 to 3, 0.3 to 4.3, 0.3 to 5.6, 1 to 4, 1 to 5.3, 2 to 4, 2 to 5.3, 3 to 6.
2. Sharp Kp decrease. We analyzed jL_{PP} values obtained for the same Kp jumps as in (1) but in opposite direction, e.g., Kp jumps from Kp = 3 to Kp = 0.3.
3. Short-time burst enhancement in Kp. We consider the Kp increase as in (1), after that Kp retains constant higher value for 3 hr and then decreases to lower values as in (2).
4. Increase-decrease in Kp. The Kp increase as in (1) retains constant higher value for 6 hr and then decrease to lower values as in (2).

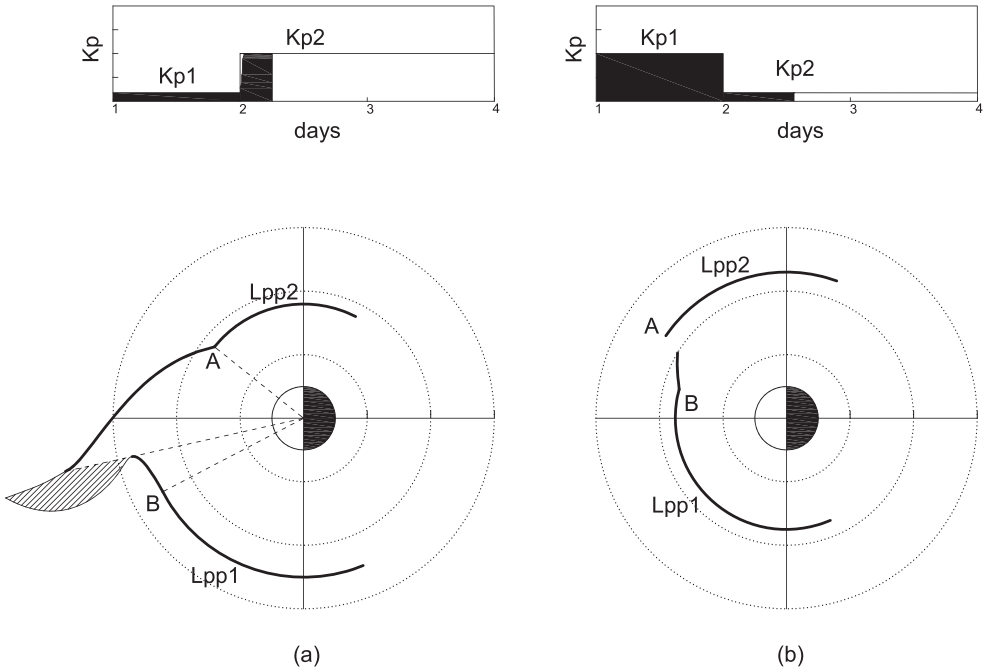

Figure 1. Schematic of the plasmapause including plasmapause structures: (a) plume and (b) shoulder. The Kp index is shown on the top. Values $L_{PP}1$ and $L_{PP}2$ are related to Kp1 and Kp2 in both shown cases. The main plasmapause is depicted as thick black and embrace $L_{PP}1$, $L_{PP}2$, and most inward border of the structures. Note that in case of the plume, the shaded area is a part of the plume, but its borders do not constitute the main plasmapause.

5. Increase-decrease in Kp. The Kp increase as in (1) retains constant higher value for 12 hr and then decrease to lower values as in (2).

Thus, we obtain five jL_{PP} data sets (thereafter subdata set (1), …, subdata set (5)), each developed by considering all eight changes of Kp values within each of the five Kp jump category. The whole data set contains 26,454 plasmapause positions. The DAY2 was examined. As mentioned above, in the study by Verbanac et al. (2018), it is described in detail how the simulated plasmapause positions were obtained. Here, we do not want to repeat the whole procedure but only explain the difference in the obtained number of plasmapause values in their work and in the present one. The data set of Verbanac et al. (2018) (data set 1) exploited 68 days. In the new data set (data set 2), we consider eight different Kp jumps with five subdata sets as explained above, corresponding to 40 days. Thus, we should obtain 27,000 plasmapause values ($675(25\times27)\times40$). Because of the data gaps (also explained in Verbanac et al., 2018), we finally have 26,454 jL_{PP} values. This data set contains enough plasmapause positions to obtain the smooth cross-correlation curves that can be compared with those obtained in Verbanac et al. (2018). The input ionospheric velocity has been chosen to be that of the corotation. Note that the perfect UT-MLT plasmapause coverage is achieved for both L_{PP} data sets: 1-hr space-time resolution.

Let us now define some terms that will be used along the paper. Figure 1 provides schematic explanation of the plasmapause including plasmapause structures and explanation of the related terms. As an example, development of the plume (Figure 1a) and shoulder (Figure 1b) is shown.

Due to the change of the Kp (from Kp1 to Kp2), the plasmapause formation is initiated in the postmidnight sector and the newly formed plasmapause, then azimuthally propagates to other MLT sectors. If Kp history is constant for at least 24 hr, plasmapause value that correspond to the Kp2 value will be transmitted to all 24 MLT sectors, and the plasmapause will be circular. The L_{PP} values for specific Kp used in this study (mentioned above) are given in Table 1. Important to note is that the formation of any structure is related to the changes in the Kp and not to some specific Kp value.

Table 1
The L_{PP} values related to the specific Kp values

Kp	L_{pp}
0.33	4.7
1	4.5
2	4.3
3	4
4	3.7
4.33	3.55
5.33	3.1
5.66	2.9
6	2.8

In the first example (Figure 1a), the L_{PP} related to the value to which Kp has increased represents the newly formed plasmapause and is denoted as $L_{PP}2$. The Sun is in the left direction (12 MLT), midnight on the right (0 MLT), the top of the figure corresponds to the dawn (6 MLT), and the bottom to the duskside (18 MLT). The plasmapause at dayside, not yet affected by the changes in the magnetospheric electric field (still not affected by the emerging/upcoming structure), attains values $L_{PP}1$. The Kp jump to the higher value (Figure 1a, top panel), from value Kp1 to a value Kp2, causes in the postmidnight sector a closer plasmapause creating a structure that evolves in a plume in the afternoon sector and then rotates to the duskside (this is also noticed in the study by Pierrard & Lemaire, 2004). Plume has azimuthal and radial extension. Azimuthal extension of the plume is defined as the azimuthal distance between the two end points of the structure (points A and B in the figure). Thus, the plume azimuthally extends between $L_{PP}1$ and $L_{PP}2$. Note that erosion of the plasmasphere occurs quickly over a timescale of half an hour to 1 hr (Bandić et al., 2017; Goldstein et al., 2003; Lemaire, 1987) causing that vestigial plasmapause does not coexist with the new one. Therefore, the simulated plasmapause is the real, newly formed one. At specific MLT, the created plume may have several radial borders. Its most inner border, together with $L_{PP}1$ and $L_{PP}2$, are referred to the main plasmapause. Note that the shaded area is a part of the plume, but its borders do not constitute the main plasmapause according to our definition.

In the second example, the Kp jump to the lower value (Figure 1b) causes a farther plasmapause. The structure, shoulder, is created in the postmidnight (details are provided in the next section) that then rotates to the duskside. The development of the new plasmapause is slower in this case. It is mainly controlled by ionospheric refilling that lasts over a period of days (Park, 1970; 1974). Therefore, because of the refilling, more plasmaspheric borders can simultaneously exist representing the vestigial and newly formed plasmapause. The simulation outputs provide the new plasmapause (the most outward one), the one formed after the refilling process is finished. Shoulder azimuthally extends from point A to point B. Note that at particular MLT sector, this structure has only one radial border. Thus, $L_{PP}1$, $L_{PP}2$, and the L_{PP} related to the shoulder are referred to the main plasmapause.

Recall that 02–05 MLT sectors embrace two simulation branches, which we separately consider. The one that we chose is the main plasmapause.

To summarize, in all cases, the main plasmapause embraces the values that the simulation gives, except in the case of the plume when the most inward simulation values are considered to be the main plasmapause.

Since we are interested in the global plasmapause behavior, we consider only the main plasmapause. In this study, these L_{PP} values, related to the main plasmapause, constitute the jL_{PP} data sets.

3. Characteristics of the Plasmapause Simulated with Kp Jumps, jL_{PP} Values

In this section, we focus on the jL_{PP} behavior obtained using different Kp jumps (explained in the previous section).

To recall, the sharp Kp increase, sharp Kp decrease, and short time burst enhancement in Kp result in development of plume, shoulder, and notch, respectively. When Kp increases, remains constant for 6 (12) hr and then decreases the plume is first formed and after 6 (12) hr the shoulder appears.

It is not possible to show all analyzed simulation outputs. Since the dynamic in the plasmapause evolution is the most prominent when Kp increases, in this case, the jL_{PP} will be displayed at 16 instants of time. For other types of Kp jumps, the jL_{PP} snapshots will be shown at four UTs.

Before focusing on specific cases, related to certain Kp jumps, we outline the common characteristics generally observed. The simulation outputs for all investigated cases clearly show that the initial plasmapause radial motion (erosion or expansion) occurs at the nightside, more intense around postmidnight. This is in accordance with the strongest E5D field in these MLT sectors, lower conductivity, but may be influenced with the simulation starts at 02 MLT (as discussed in detail in Verbanac et al., 2018). For different changes in the E-Field (different Kp jumps: e.g., Kp increase and Kp decrease), the formation of the new plasmapause

can be noted in slightly different night MLT sectors (this will be noted below when describing main plasmapause with specific structures). Further, all simulations show eastward rotation of the whole plasmapause (main plasmapause and the developed structures).

In Figures 2 and 3, we show some of the simulation outputs related to above explained five types of Kp jumps. We present here the cases where Kp value changes (increase, decrease) between 1 and 4. According to Table 1, the simulations provide $L_{PP} = 4.5$ for Kp = 1 and $L_{PP} = 3.7$ for Kp = 4. Following the explanation and definition given in the previous section for the example of plume formation these first and second L_{PP} values correspond to $L_{PP}1$ and $L_{PP}2$, respectively. The plasmapause in the geomagnetic equatorial plane is displayed at some instants of time in "DAY2". As mentioned previously, this is because the Kp history during the previous 24 hr determines the plasmapause in the interchange mechanism. The related geomagnetic Kp index is also shown.

At the nightside sectors, from MLT21 to MLT02, the simulation outputs do not provide two plasmapause branches, and it seems as the plasmapause is "static". But, it does not mean that the dayside ("old") plasmapause had not rotated to these sectors. Namely, the constant E-field constantly pushes the plasmapause to the value that is related to the specific Kp value what is actually physical and seen in the simulation snapshots.

In the following, we analyze and provide more details on the characteristics of the main plasmapause with plume, shoulder, notch, and finally, the main plasmapause with plume and shoulder that exist simultaneously as separate structures.

3.1. Main Plasmapause with Plume

Development and evolution of plume is presented in Figure 2. At UT = 0 at DAY2, plasmapause is circular with the value that corresponds to Kp = 1. The radial movement that denotes the formation of the new plasmapause is first seen around 2 MLT at 0.5 UT. Soon after the start of the plasmapause erosion the radial plasmapause motions are observed in the nightside, already from 21 MLT. After about 1.5 hr, the development of the structure that starts to evolve in the plume at dawnside (after about 3 hr) is noticed. As the main plasmapause and the whole structure rotate eastward, the plume begins to deform both radially (radial extension with sunward tail formation) and azimuthally. As mentioned above, the radial development of the plume is not analyzed since we are interested in the evolution and characteristics of the main plasmapause. The evolution of the plume (accordingly its main part in which we are interested) is accompanied with azimuthal widening. Depending on the investigated increase of Kp value, the plume can achieve the azimuthal extension of about 4–8 MLTs in the predusk sectors. For the shown example, the maximal plume extension is about 5 MLTs (see Figure 2). We note that for lower Kp jumps (e.g., Kp changes Kp jump between 0.3 and 3) the formed plumes do not deform drastically and are less azimuthally extended. In all cases, we observed the disintegration of plumes in the postdusk sectors. After 24 hr of constant Kp, plasmapause is again circular with the value related to the Kp = 4 (see the last plot in the figure, UT = 23.5).

3.2. Main Plasmapause with Shoulder

The formation of the new plasmapause can be followed from about 23 MLT (slightly seen at second panel of Figure 3a). The radial movements in all MLT sectors are generally less prominent than that in the case of Kp increase. Also note that the radial motions when Kp increase are seen earlier in MLTs (from 21 MLT). Shoulder has the initial azimuthal extension of about 1 MLT, and this width remains approximately unchanged during its lifetime. This is valid for all investigated Kp decreases. Accordingly, widening and significant shoulder deformation on the dayside is not observed. Interestingly the shoulder disintegration in the postdusk is not visible. The reason is the same as we will explain in the following, for the notch.

3.3. Main Plasmapause with Notch

This case is shown in Figure 3b. Soon after the initial plasmapause erosion formation of the plume is seen. The plume does not fully develop as when we have only Kp increase (explained above), because after 3 hr the shoulder is formed and limit further deformation of the plume. Note that plume and shoulder together constitute one structure, the notch, which rotates eastward. Tail is not developed. The notch is well visible at premidnight. The disintegration of the plume starts at postmidnight, as expected. Namely, the development of the plume is limited by appearance of the shoulder. Further, the decrease of Kp means that the E-field becomes less intense and consequently also the inward radial movement decreases. As result, the plume can still exist in the premidnight sector.

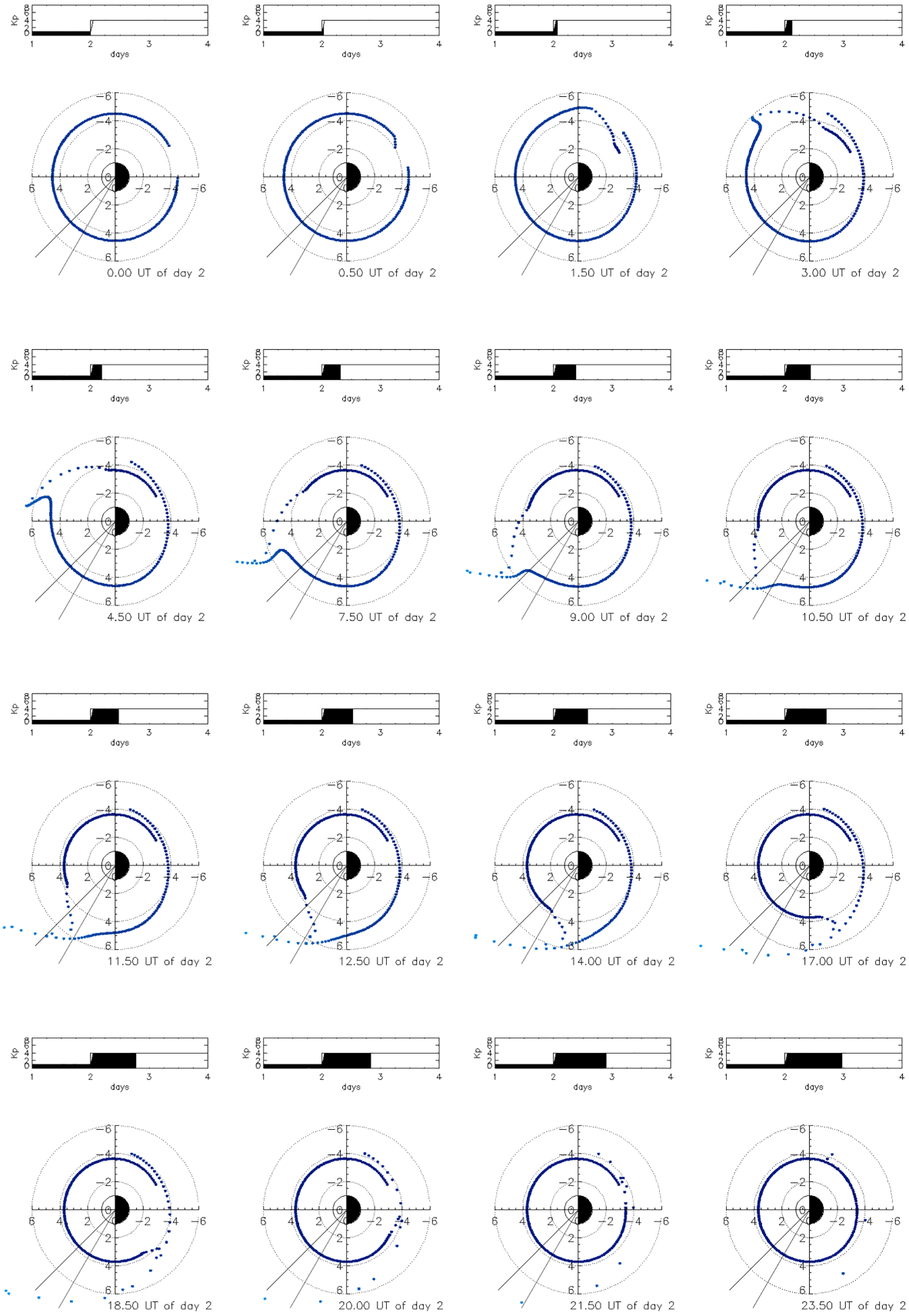

Figure 2. An example of the simulation output at 16 instants of time. Kp index is shown on the top. Kp value increases from Kp = 1 to Kp = 4 at UT = 0.

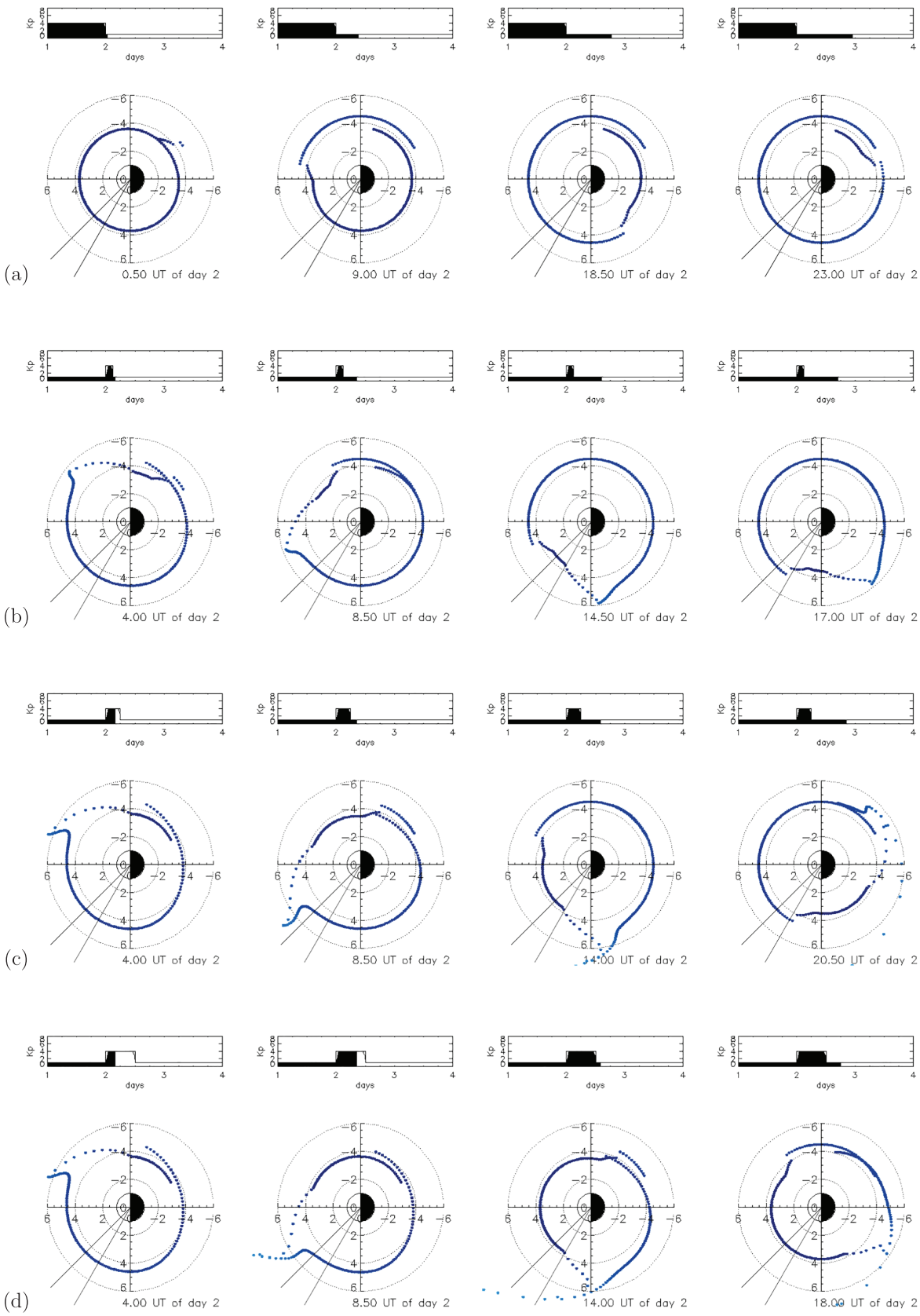

Figure 3. An example of the simulation output at four instants of time. Kp index is shown on the top. (a) Kp value decreases from Kp = 4 to Kp = 1 at UT = 0, (b)–(d) Kp increases from Kp = 1 to Kp = 4 at UT = 0, retains constant higher value for 3, 6, and 12 hr respectively, and then decreases again to Kp = 1.

3.4. Main Plasmapause with Plume and Shoulder

We show cases when Kp remains constant 6 hr (Figure 3c) and 12 hr (Figure 3d). All panels in Figures 3c and 3d reveal the formation of the plume soon after the initial plasmapause erosion. Plume is again well developed at dayside. As Kp starts to decrease, the shoulder appears. The plume and shoulder exist simultaneously as separate structures. Two structures rotate 6/12 MLTs apart of each other. The extension of the plume becomes stable (unchanged) once the shoulder is developed. In both cases, tail is visible and the plume disintegrates in the postmidnight sector. The reason is the same as we have explained above, for the notch.

4. Analyses of the CC Curves

To study the response of the main plasmapause to the changes in the E-field, we investigate the relationship between the chosen PP indicator Kp and both sL_{PP} and jL_{PP} by applying the cross-correlation analysis. This PP indicator is employed because the jL_{PP} data set is actually constructed considering the changes in the Kp values (Kp jumps) as described in section 2.

We follow the work by Verbanac et al. (2015). The readers are referred to that paper for more details. Shortly, the CC functions are obtained up to a time lag (T_{lag}) of 30 hr with a step of 1 hr. The T_{lag} is referred to as the time that the plasmasphere needs to react to the changes of the E-field in the specific MLT sector. As results of the applied method to sL_{PP} and jL_{PP} data sets, we obtain the CC curves that we utilize to reveal the MLT dependence of the plasmapause evolution and dynamics.

Here, we recall that the CC curves related to sL_{PP} values and different PP indicators (related to both solar wind parameters and following geomagnetic indices AE, Ap, and Dst) are shown and analyzed in work by Verbanac et al. (2018). They noticed the constant parts and T_{lag} belts in the CC curves. The T_{lag} belt is defined as a width of valleys/mountains in the CC curve that embraces T_{lag} values around the maximal T_{lag}. They argued that the plasmapause formation may occur in the few MLTs simultaneously, between 21 and 07 MLTs. The T_{lag} belts are interpreted as the evidence of MLT range of the plasmapause formation. In our case, the PP indicator is Kp, and consequently, only valleys are noticed in the CC curves.

Note that jL_{PP} CC curves are constant after $T_{lag} = 25$ hr, since we have examined only DAY2 of the simulation outputs. Namely, the last change in Kp could occur maximally 25 hr before the chosen UT hour of DAY 2.

In the following the sL_{PP} and jL_{PP} CC curves obtained in each of the 1-hr MLT bins within 25 hr are analyzed and compared with each other. Then, we focus on the characteristics of the jL_{PP} CC curves.

4.1. Comparison of the sL_{PP} and jL_{PP} CC Curves

Now, we compare the sL_{PP} with jL_{PP} CC curves. The CC curves derived from individual subdata sets ([1], [2], and [3]) and combined subdata sets ([1]–[3] and [1]–[5]) are investigated within each 1-bin MLT sectors. Recall that data sets (1)–(5) are related to the Kp increase, Kp decrease, short-time Kp burst, 6-hr Kp burst, and 12-hr Kp burst, respectively.

As an example, we show and discuss here the CC curves related to 15–16 MLT sector that are shown in Figure 4. This MLT sector is representative because there the evolution (related to both the rotation and radial deformation) of the structure formed in the postmidnight can be followed. Moreover, some case studies (e.g., Goldstein, Burch, et al., 2005; Goldstein, Sandel, et al., 2005) described development of the structures in the dayside.

First three plots in the figure are related to the sharp Kp increase, sharp Kp decrease, and short-time burst enhancement in Kp, respectively (subdata sets [1]–[3]). We see that each of these individual data sets cannot completely explain the sL_{PP} CC curve that is shown in the forth and fifth plots, depicted in grey. If only two of the three subdata sets, (1)-(3), are combined a resemblance between the obtained jL_{PP} and sL_{PP} CC curves could not be established. When these three data sets are merged, a very good resemblance between the obtained jL_{PP} and sL_{PP} CC curves is achieved as can be seen in the fourth plot (jL_{PP} CC curve is shown in tick black). This indicates that to reproduce the sL_{PP} CC curves, we have to combine minimally three types of Kp jumps (subdata sets [1]–[3]), which cause development of plumes, shoulders, and notches, respectively. The good match is especially seen around the maximum of the CC curves, which is actually the physically important part of the CC curves. Namely, in every cross-correlation analysis (also taking the most simple case when two arrays are cross-correlated), the values around the maximal correlation are the important ones.

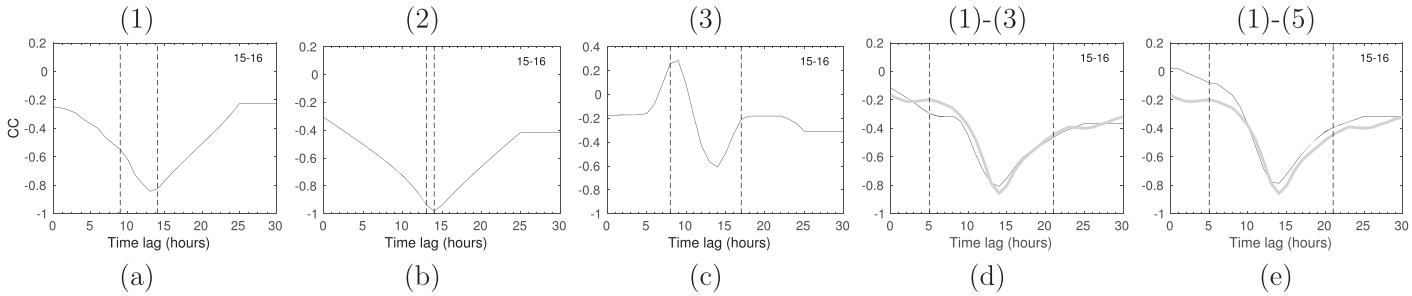

Figure 4. Cross-correlation function describing the Kp-jL_{PP} relationship (a)–(c) derived from individual subdata sets (1), (2), and (3), (d) combined subdata sets (1)–(3), and (e) combined subdata sets (1)–(5). Cross-correlation function describing the Kp-sL_{PP} relationship are overplotted (depicted as grey) in panels (d) and (e). The 15–16 MLT sector is shown. Vertical lines denote *Tlag-S* in panels (a)–(c) and the T_{lag} belts in panels (d) and (e). The numbers on the top of each panel denote the used data set (see section 2 for details).

This means that the combined subdata sets (1)–(3) are sufficient to explain the sL_{PP} CC curve. Inspection of the CC curves for 27 MLT sectors (24 MLTs of the first and 3 MLTs of the second simulation cycle) given in the supporting information reveals that this is valid for all examined MLT sectors.

We anticipated that the matching of the sL_{PP} and jL_{PP} CC curves can be improved in the whole range of T_{lag} values by including combinations of up and down Kp jumps separated in time. To check that we employed the additional types of Kp-jumps, subdata sets (4) and (5), which include Kp increase at UT = 0 and then Kp decrease at UT = 6 and UT = 12, respectively. Therefore, we constructed the CC curves using all five types of Kp jumps (subdata sets [1]–[5]). These CC curves are presented in the fifth plot, depicted as black.

Generally, looking at all MLT sectors, the best match between jL_{PP} and sL_{PP} CC curves is attained (not necessarily in each MLT sector) when all five jL_{PP} subdata sets are combined. Again, the best similarity is seen around the maximal T_{lag}, as expected, but improvement is also seen at the part of the CC curves that are more apart from the maximum. If we would additionally add more types of Kp jumps separated in time (other than subdata sets [4] and [5]), probably even better match between the sL_{PP} and jL_{PP} CC curves could be achieved. For the purpose of this study, it is not needed since the important part of the CC curves are those around the maximal T_{lag} values where the good similarities are already achieved. Actually, with combining subdata sets (4) and (5) satisfying agreement is obtained between all parts of the CC curves.

As already noted, the jL_{PP} CC curves are constant after $T_{lag} = 25$ hr. But the same trend of the jL_{PP} and sL_{PP} CC curves up to 25 hr suggests continuation of the observed similarity also beyond $T_{lag} = 25$ hr.

4.2. Characteristics of the jL_{PP} CC Curves

Now, when we have the jL_{PP} CC curves that are in agreement with sL_{PP} CC curves for which we exactly know how they are obtained, we will try to provide understandings and details of their behavior. To recall, the sL_{PP} values are obtained using real Kp values (thus, real arbitrary Kp jumps). On the other side, jL_{PP} values result from specific Kp jumps that we have explicitly defined.

In the following, we analyze the characteristics of the CC curves obtained from jL_{PP} values by inspecting the simulation outputs (snapshots) at some UTs shown in Figures 2 and 3. We focus again on 15–16 MLT sector that is marked with lines in these figures. Time of the structure passages through this MLT sector is estimated to be 9–14 UT, 13–14 UT, and 9–17 UT for plume, shoulder, and notch, respectively. Assuming that the plasmapause at all MLTs azimuthally propagates with the mean angular velocity close to corotation (as suggested by Verbanac et al., 2018), this is equivalent to the azimuthal extension of these structures that account for ΔMLT = 5, ΔMLT = 1, and ΔMLT = 8 for plume, shoulder, and notch, respectively.

Inspecting their CC curves (plots [a]–[c]) in Figure 4), we find that the correlation maximums are placed within T_{lag} intervals that correspond to the mentioned UT intervals. These T_{lag} intervals will be called *Tlag-S*, and they are denoted by vertical dashed lines in Figures 4a–4c. At some time, the Kp jump occurs, and the related structure is formed at postmidnight. Then, there is a time needed for the structure to arrive from its formation sector to the investigated 15–16 MLT sector. This time represents the start time of *Tlag-S*. As the structure passes through this MLT sector, the correlation starts to change as expected. The end time of the *Tlag-S* is the time when the structure leaves the MLT sector. Therefore, we can notice that *Tlag-S* has the width that corresponds to the azimuthal extension of the structure.

We remind the reader that the values estimated from the investigated snapshots (Figures 2 and 3) are related to Kp jumps between 1 and 4. The CC curves shown in Figure 4 are derived including all eight changes of Kp values within each subdata sets. Therefore, the above mentioned times and azimuthal extensions of the structures may not be exactly the same as the T_{lag} interval (*Tlag-S*).

The T_{lag} range depicted with vertical dashed lines in Figure 4d is actually the T_{lag} belt that is obtained when subdata sets (1)–(3) are combined, and it reflects the existence of *Tlag-S*. When all subdata sets ([1]–[5]) are employed, the obtained CC curves again provide statistical information on the width of the T_{lag} belt (shown as vertical dashed lines in Figure 4e).

5. Discussion and Conclusion

We have investigated the jL_{PP} derived from interchange instability mechanism for the cases of the sharp Kp increase, sharp Kp decrease, short-time burst enhancement in Kp, increase-decrease in Kp when Kp retains constant high value for 6/12 hr, and then decrease to lower values. The related CC curves were compared with sL_{PP} curves obtained by using real Kp values. Recall that the sL_{PP} curves for different PP indicators are in well agreement with experimental CC curves based on THEMIS observations, as shown by Verbanac et al. (2018). The comparison is investigated in 27 MLT sectors (24 MLTs of the first and 3 MLTs of the second simulation cycle). It is demonstrated that each individual Kp jump, Kp increase, Kp decrease, and short-time burst enhancement in Kp cannot fully reproduce the sL_{PP} curves. We have shown that it is possible to achieve the very good match between the sL_{PP} and jL_{PP} CC curves already when three types of Kp jumps that allow development of plume, shoulder, and notch are combined. Further, to investigate the possible improvement in the match of sL_{PP} and jL_{PP} CC curves, we employed all five types of Kp jumps (with all eight changes of Kp values). The T_{lag} belts are noted in both CC curves obtained combining subdata sets (1)–(3) and subdata sets (1)–(5). The characteristics of the jL_{PP} CC curves were studied by analyzing the simulation snapshots. They reveal the circular plasmapause when Kp is constant for at least 24 hr, plasmapause erosion at nightside, development of the structure soon after Kp has changed at the nightside, eastward rotation of the main plasmapause and related structure, and azimuthal development of the structure (also its radial development that has not been analyzed in this study). The T_{lag} belts in the CC curves are interpreted as the imprint of the plasmapause structure passages through specific MLT sector. Thus, the width of T_{lag} values affected by the changes in the correlation reflects the azimuthal extension of the structure. On the other side, the results by Verbanac et al. (2018) suggested that the T_{lag} belts reflect the MLT range of the plasmapause formation. Since both results seem to be physically plausible, and not necessarily exclusive, we suggest that this issue has to be further investigated.

Different PP structures observed in nature are signature of the complex processes that cause the formation and evolution of the plasmapause. Based on the studies that have been performed so far utilizing different data sets, methods, and theories, it seems difficult to describe the global plasmapause behavior without employing various and complex physical processes. Analyzing the characteristics of the main plasmapause over longer time period (that includes a lot of events), we succeed to simplify and systematize the global plasmapause behavior. This study has shown that with employing only three types of Kp jumps (sharp Kp increase, sharp Kp decrease, short-time burst enhancement in Kp), and the theory based on interchange instability mechanism, the formation and evolution of the main plasmapause can be statistically explained. This implies that these Kp jumps are probably the most frequently occurring. Moreover, the structures related to the mentioned Kp changes are most frequently observed in nature (e.g., in the Extreme UltraViolet images) supporting our indications.

Although the plasmapause in the single events shows very complex and different behaviors, we have obtained the global plasmapause evolution in time (azimuthal propagation and MLT sectors of radial deformation). The simple explanation of what causes such plasmapause global motions is the most important findings of our study.

Acknowledgments
We thank Damir Hržina and Josip Modrić for helping in figure preparation. The authors wish to thank Joseph Lemaire for his useful comments and suggestions. The authors further thank all the staff members providing the geomagnetic index Kp available at https://www.ngdc.noaa.gov. V. Pierrard thanks the Solar-Terrestrial Center of Excellence. The SPM plasmasphere and plasmapause model used in the recent study is available on Space Situational Awareness: http://swe.ssa.esa.int/space-radiation (on this page with the title "Space Radiation Expert Service Centre (R-ESC)" choose the Tab "Contributions" → BIRA-IASB Space Weather Services (BIRA-IASB) → SPM (SWIFF Plasmasphere (SPM) electron density distribution model).

References

André, N., & Lemaire, J. F. (2006). Convective instabilities in the plasmasphere. *Journal of Atmospheric and Solar-Terrestrial Physics*, *68*(2), 213–227. https://doi.org/10.1016/j.jastp.2005.10.013

Bandić, M., Verbanac, G., Moldwin, M. B., Pierrard, V., & Piredda, G. (2016). MLT dependence in the relationship between plasmapause, solar wind and geomagnetic activity based on CRRES: 1990-1991. *Journal of Geophysical Research: Space Physics*, *121*, 4397–4408. https://doi.org/10.1002/2015JA022278

Bandić, M., Verbanac, G., Pierrard, V., & Cho, J. (2017). Evidence of MLT propagation of the plasmapause inferred from THEMIS data. *Journal of Atmospheric and Solar-Terrestrial Physics*, *161*, 55–63. https://doi.org/10.1016/j.jastp.2017.05.005

Darrouzet, F., De Keyser, J., & Pierrard, V. (2009). *The Earth's plasmasphere: A Cluster and IMAGE perspective*. New York: Springer. https://doi.org/10.1007/978-1-4419-1323-4

Darrouzet, F., Gallagher, D. L., André, N., Carpenter, D. L., Dandouras, I., Décréau, P. M. E., et al. (2009). Plasmaspheric density structures and dynamics: Properties observed by the Cluster and IMAGE missions. *Space Science Reviews*, *145*(1-2), 55–106. https://doi.org/10.1007/s11214-008-9438-9

Ferriere, K. (2001). Interchange, quasiinterchange, ballooning modes: What is their exact definition? *Eos, Transactions American Geophysical Union*, *82*(38), 420–421. https://doi.org/10.1029/01EO00260

Gallagher, D. L., Adrian, M. L., & Liemohn, M. W. (2005). Origin and evolution of deep plasmaspheric notches. *Journal of Geophysical Research*, *110*, A09201. https://doi.org/10.1029/2004JA010906

Gold, T. (1959). Motions in the magnetosphere of the Earth. *Journal of Geophysical Research*, *64*, 1219–1224. https://doi.org/10.1029/JZ064i009p01219

Goldstein, J., Burch, J. L., Sandel, B. R., Mende, S. B., C:Son Brandt, P., & Hairston, M. R. (2005). Coupled response of the inner magnetosphere and ionosphere on 17 April 2002. *Journal of Geophysical Research*, *110*, A03205. https://doi.org/10.1029/2004JA010712

Goldstein, J., Sandel, B. R., Forrester, W. T., & Reiff, P. H. (2003). IMF-driven plasmasphere erosion of 10 July 2000. *Geophysical Research Letters*, *30*(3), 46–1. https://doi.org/10.1029/2002GL016478

Goldstein, J., Sandel, B., Forrester, W., Thomsen, M., & Hairston, M. (2005). Global plasmasphere evolution 22-23 april 2001. *Journal of Geophysical Research*, *110*, A12218. https://doi.org/10.1029/2005JA011282

Horwitz, J. L., Comfort, R. H., & Chappell, C. R. (1990). A statistical characterization of plasmasphere density structure and boundary locations. *Journal of Geophysical Research*, *95*, 7937–7947. https://doi.org/10.1029/JA095iA06p07937

Huba, J. D., & Sazykin, S. (2017). SAMI3-RCM simulation of the 17 March 2015 geomagnetic storm. *Journal of Geophysical Research: Space Physics*, *122*, 1246–1257. https://doi.org/10.1002/2016JA023341

Lambour, R. L., Weiss, L. A., Elphic, R. C., & Thomsen, M. F. (1997). Global modeling of the plasmasphere following storm sudden commencements. *Journal of Geophysical Research*, *102*(A11), 24,351–24,368. https://doi.org/10.1029/97JA02037

Lemaire, J. (1987). The plasmapause formation. *Physica Scripta Volume T*, *18*, 111–118. https://doi.org/10.1088/0031-8949/1987/T18/012

Lemaire, J. F., & Gringauz, K. I. (1998). *The earth's plasmasphere*. New York: Cambridge University Press.

McIlwain, C. E. (1986). A Kp dependent equatorial electric field model. *Advances in Space Research*, *6*(3), 187–197. https://doi.org/10.1016/0273-1177(86)90331-5

Park, C. G. (1970). Whistler observations of the interchange of ionization between the ionosphere and the protonosphere. *Journal of Geophysical Research*, *75*, 4249–4260. https://doi.org/10.1029/JA075i022p04249

Park, C. G. (1974). Some features of plasma distribution in the plasmasphere deduced from Antarctic whistlers. *Journal of Geophysical Research*, *79*, 169–173. https://doi.org/10.1029/JA079i001p00169

Pierrard, V., & Cabrera, J. (2005). Comparisons between EUV/IMAGE observations and numerical simulations of the plasmapause formation. *Annales Geophysicae*, *23*(7), 2635–2646. https://doi.org/10.5194/angeo-23-2635-2005

Pierrard, V., & Cabrera, J. (2006). Dynamical simulations of plasmapause deformations. *Space Science Reviews*, *122*(1-4), 119–126. https://doi.org/10.1007/s11214-005-5670-8

Pierrard, V., Khazanov, G. V., Cabrera, J., & Lemaire, J. (2008). Influence of the convection electric field models on predicted plasmapause positions during magnetic storms. *Journal of Geophysical Research*, *113*, A08212. https://doi.org/10.1029/2007JA012612

Pierrard, V., & Lemaire, J. (2004). Development of shoulders and plumes in the frame of the interchange instability mechanism for plasmapause formation. *Geophysical Research Letters*, *31*, L05809. https://doi.org/10.1029/2003GL018919

Pierrard, V., & Stegen, K. (2008). A three-dimensional dynamic kinetic model of the plasmasphere. *Journal of Geophysical Research*, *113*, A10209. https://doi.org/10.1029/2008JA013060

Sandel, B. R., Goldstein, J., Gallagher, D. L., & Spasojevic, M. (2003). Extreme ultraviolet imager observations of the structure and dynamics of the plasmasphere. *Space Science Reviews*, *109*, 25–46. https://doi.org/10.1023/B:SPAC.0000007511.47727.5b

Sheeley, B. W., Moldwin, M. B., Rassoul, H. K., & Anderson, R. R. (2001). An empirical plasmasphere and trough density model: CRRES observations. *Journal of Geophysical Research*, *106*, 25,631–25,642. https://doi.org/10.1029/2000JA000286

Spasojević, M., Goldstein, J., Carpenter, D. L., Inan, U. S., Sandel, B. R., Moldwin, M. B., & Reinisch, B. W. (2003). Global response of the plasmasphere to a geomagnetic disturbance. *Journal of Geophysical Research*, *108*(A9), 1340. https://doi.org/10.1029/2003JA009987

Verbanac, G., Bandić, M., Pierrard, V., & Cho, J. (2018). MLT plasmapause characteristics: Comparison between THEMIS observations and numerical simulations. *Journal of Geophysical Research: Space Physics*, *123*, 2000–2017. https://doi.org/10.1002/2017JA024573

Verbanac, G., Pierrard, V., Bandić, M., Darrouzet, F., Rauch, J. L., & Décréau, P. (2015). Relationship between plasmapause, solar wind and geomagnetic activity between 2007 and 2011. *Annales Geophysicae*, *33*, 1271–1283. https://doi.org/10.5194/angeo-33-1271-2015